Constraining isocurvature perturbations with the 21 cm emission from minihaloes

Yoshitaka Takeuchi[1]★ and Sirichai Chongchitnan[2]

[1]*Department of Physics, Nagoya University, Naogya 464-8602, Japan*
[2]*Department of Physics and Mathematics, University of Hull, Cottingham Road, Hull HU6 7RX, UK*

ABSTRACT

We investigate the effects of isocurvature perturbations on the 21 cm radiation from minihaloes (MHs) at high redshifts and examine constraints on the isocurvature amplitude and power spectrum using the next generation of radio telescopes such as the Square Kilometre Array. We find that there is a realistic prospect of observing the isocurvature imprints in the 21 cm emission from MHs, but only if the isocurvature spectral index is close to 3 (i.e. the spectrum is blue). When the isocurvature fraction increases beyond ∼10 per cent of the adiabatic component, we observe an unexpected decline in the 21 cm fluctuations from small-mass MHs, which can be explained by the incorporation small MHs into larger haloes. We perform a detailed Fisher-matrix analysis and conclude that the combination of future cosmic microwave background and 21 cm experiments (such as *CMBPol* and the Fast Fourier Transform Telescope) is ideal in constraining the isocurvature parameters, but will stop short of distinguishing between cold dark matter and baryon types of isocurvature perturbations, unless the isocurvature fraction is large and the spectrum is blue.

Key words: cosmology: theory – diffuse radiation – radio lines: general.

1 INTRODUCTION

Recent measurements of the anisotropies in the cosmic microwave background (CMB) by the *Planck* satellite have placed constraints of unprecedented accuracy on the amplitude of the primordial density fluctuations (Planck Collaboration 2013a,b). Planck also revealed that these fluctuations are consistent with having originated from *adiabatic* initial conditions, characterized by the constancy of the ratios of density contrasts of various particle species in the early Universe (see Bardeen 1980; Kodama & Sasaki 1984 for reviews). This is in agreement with previous CMB measurements by the *Wilkinson Microwave Anisotropy Probe* satellite (Bennett et al. 2013; Hinshaw et al. 2013). On the other hand, if the aforementioned ratios of density contrasts are *not* constant, the fluctuations are said to be generated from *isocurvature* initial conditions, of which there are four types, namely, the cold dark matter (CDM), baryon, neutrino-density and neutrino-velocity isocurvature perturbations (Bucher, Moodley & Turok 2000). Constraints from Planck limit any isocurvature contributions to the CMB temperature anisotropies to less than ∼10 per cent.

The simplest model of inflation involving a single, slowly rolling scalar field predicts that density fluctuations are generated from purely adiabatic initial conditions. Hence, the detection of any

isocurvature contribution would be a window to novel physical mechanisms in the inflationary era. Such mechanisms include the curvaton mechanism (Langlois & Vernizzi 2004; Lazarides, de Austri & Trotta 2004; Moroi & Takahashi 2005; Moroi, Takahashi & Toyoda 2005; Ichikawa et al. 2008a; Langlois, Vernizzi & Wands 2008), the axion and gravitino CDM (Rajagopal, Turner & Wilczek 1991; Covi et al. 2001; Covi, Roszkowski & Small 2002; Brandenburg & Steffen 2004) and the modulated reheating scenarios (Kofman 2003; Dvali, Gruzinov & Zaldarriaga 2004; Ichikawa et al. 2008b; Takahashi, Yamaguchi & Yokoyama 2009a; Takahashi et al. 2009b) as well as various combinations of such scenarios. In most of these models, a large isocurvature fraction can be produced at the expense of the introduction of a few additional parameters (Moroi & Takahashi 2002, 2009; Lyth & Wands 2003; Lyth, Ungarelli & Wands 2003; Beltran 2008; Takahashi et al. 2009b).

According to our current understanding of cosmology, inflation-stretched primordial quantum fluctuations subsequently grow via gravitational instability into the observed cosmic structures. One of the earliest cosmic structures to form were minihaloes (MHs), which are virialized haloes of dark and baryonic matter with typical mass 10^4–10^8 M$_\odot$ and temperature $\lesssim 10^4$ K, at very high redshift ($z \sim 6$–20). MHs typically host a high density of neutral hydrogen, which can be detected by the 21 cm absorption/emission line due to the transition of the hydrogen atom from a parallel to antiparallel spin state. MHs are typically at such high temperatures that their 21 cm signal appears in emission with respect to the CMB (Iliev

★ E-mail: yoshitaka@nagoya-u.jp

et al. 2002). The 21 cm signals from MHs give us information on the small-scale density fluctuations at high redshifts, and their detection will therefore lead to a deeper understanding of small-scale physics during the earliest structure formation epoch.

The 21 cm signal from MHs has previously been studied by Chongchitnan & Silk (2012b), who showed that the 21 cm emissions from MHs are a sensitive probe of primordial non-Gaussianity, due to a strong dependence of the MH number density and bias on the amplitude of non-Gaussianity. Tashiro, Sekiguchi & Silk (2013) calculated the 21 cm fluctuations due to MHs in cosmic wakes produced by cosmic strings.

In this paper, we present a new probe of isocurvature fluctuations using the 21 cm signal from MHs. We will show that the fluctuations in the 21 cm emission from MHs are a viable probe of isocurvature fluctuations. We also give forecasts on the isocurvature fraction and spectral index using the next generation of large arrays of radio interferometers, which are expected to measure the cosmic 21 cm signals over a wide range of redshifts, from the cosmic dark ages ($z \sim 30$–50) down to the epoch of reionization (EoR) at $z \sim 6$. Such radio surveys include: the Low-Frequency Array (LOFAR),[1] the Murchion Widefield Array[2] and the Giant Metrewave Radio Telescope,[3] all of which focus on $6 \lesssim z \lesssim 30$, as well as more ambitious future arrays such as the Square Kilometre Array (SKA),[4] and the Fast Fourier Transform Telescope (FFTT; Tegmark & Zaldarriaga 2009), which can probe the radio Universe at $z \gtrsim 30$.

There have only been a handful of works exploring the link between 21 cm cosmology and isocurvature perturbations: Barkana & Loeb (2005) and Lewis & Challinor (2007) discussed the prospects for differentiating between the CDM and baryon isocurvature fluctuations using 21 cm signals. Further work by Kawasaki, Sekiguchi & Takahashi (2011) showed that 21 cm surveys can effectively probe the difference between CDM and baryon isocurvature fluctuations if the spectrum of isocurvature perturbations is strongly blue tilted (we revisit this claim later). Gordon & Pritchard (2009) investigated the constraints on isocurvature modes from 21 cm observations, focusing on the so-called compensated isocurvature perturbations.

This paper is organized as follows: we summarize the 21 cm radiation from MHs and its sensitivity to the presence of isocurvature modes in Section 2. The effects of isocurvature modes on the *fluctuations* of this signal are explained in Section 3. Forecasts on the constraints of isocurvature parameters from future radio surveys are discussed in Sections 4 and 5. Finally, Sections 6 and 7 contain further discussions and a summary of our main conclusions.

Throughout this work, we assume a flat Universe and adopt the cosmological parameters from Planck (Planck Collaboration 2013c).

2 21 CM EMISSION FROM MINIHALOES

The 21 cm spectral line can appear in either emission or absorption against the CMB depending on the spin temperature, T_s, determined by the balance between collisional and radiative excitations of the hydrogen atoms. The interactions between a hydrogen atom and photons, electrons and other atoms couple the spin temperature to

the temperatures of the surrounding gas and radiation field as (Field 1958)

$$T_s = \frac{T_{CMB} + y_\alpha T_\alpha + y_c T_k}{1 + y_\alpha + y_c},$$ (1)

where T_α is the colour temperature of Lyα photons, T_k is the kinetic temperature, and y_α and y_c are the radiative and collisional excitation efficiencies (Madau, Meiksin & Rees 1997). We assume that bright UV and X-ray sources have yet to form or that the MHs are isolated from such sources. Thus, we can neglect the radiative coupling and set $y_\alpha = 0$.

The amplitude of the 21 cm signal from a virialized halo depends on the density profile, velocity and temperature of the halo. We adopt as our model the *truncated isothermal sphere* (TIS; Shapiro, Iliev & Raga 1999; Iliev & Shapiro 2001), in which a MH of a given mass is described by its radius r_t, temperature T_k, density profile $\rho(r)$ and velocity dispersion σ_V. In this model, each MH is modelled as a non-singular sphere of dark matter and baryons in virial and hydrostatic equilibrium, so that $\rho(r)$ describes both the dark matter and gas profiles.

The observed brightness temperature along a line of sight, through a halo at comoving distance r from the centre of the halo, is given by

$$T_b(r) = T_{CMB}(z)e^{-\tau(r)} + \int_0^{\tau(r)} T_s e^{-\tau'} d\tau',$$ (2)

where $\tau(r)$, the total optical depth of neutral hydrogen to photons at frequency ν, can be expressed as (Furlanetto & Loeb 2002)

$$\tau(\nu) = \frac{3c^2 A_{10} T_*}{32\pi \nu_0^2} \int_{-\infty}^{\infty} \frac{n_{H_I}(\ell)\phi(\nu, \ell)}{T_s(\ell)} dR.$$ (3)

Here, R and ℓ are radial comoving distances satisfying $\ell^2 = R^2 + (\alpha r_t)^2$; α is the impact parameter in unit of r_t and n_{H_I} is the number density of neutral hydrogen. $\phi(\nu)$ is the intrinsic Doppler-broadened line profile given by

$$\phi(\nu) = \frac{1}{\Delta\nu\sqrt{\pi}} \exp\left[-\left(\frac{\nu - \nu_0}{\Delta\nu}\right)^2\right],$$ (4)

with $\Delta\nu = (\nu_0/c)\sqrt{2k_B T_k/m_H}$.

When the line profile is unbroadened; $\phi(\nu) = \delta(\nu - \nu_0)$, the optical depth corresponds to that of the Intergalactic medium (IGM) at redshift z and can be expressed as (Madau et al. 1997)

$$\tau_{IGM}(\nu; z) = \frac{3c^3 A_{10} T_* n_{H_I}(z)}{32\pi \nu_0^3 T_s(z) H(z)},$$ (5)

where A_{10} and ν_{10} are the spontaneous decay rate and the rest-frame frequency for the 21 cm transition, T_* is the equivalent temperature defined as $T_* \equiv h_p \nu_{10}/k_B$. The total optical depth can be written as

$$\tau(\nu, R) = \tau_{IGM}(\nu) + \frac{3c^2 A_{10} T_*}{32\pi \nu_0^2} \int_{-\infty}^{R} \frac{n_{H_I}(\ell')\phi(\nu, \ell')}{T_s(\ell')} dR'.$$ (6)

The first and second terms represent the contributions from IGM and the MH, respectively.

The differential 21 cm brightness temperature, δT_b, measured with respect to the CMB temperature, is given by

$$\delta T_b = \frac{1}{1+z}\left(\frac{\int dA T_b(r)}{A} - T_{CMB}(z)\right),$$ (7)

[1] http://www.lofar.org
[2] http://www.mwatelescope.org
[3] http://gmrt.ncra.tifr.res.in
[4] http://www.skatelescope.org

where T_b is averaged over the halo cross-section $A = \pi r_t^2$. The mean 21 cm emission from an ensemble of MHs in the mass range $[M_{min}, M_{max}]$ is thus given by (Iliev et al. 2002)

$$\overline{\delta T_b} = \frac{c(1+z)^4}{\nu_0 H(z)} \int_{M_{min}}^{M_{max}} \Delta\nu_{eff}\delta T_b(M)A \frac{dn}{dM}dM, \quad (8)$$

where $\nu_{eff} = [\phi(\nu_0)(1+z)]^{-1}$ is the effective redshifted line width. We take M_{max} to be the virial temperature corresponding to temperature, 10^4 K and M_{min} to be the Jeans mass, M_J.

The rms fluctuations in the 21 cm emission for a pencil-beam survey with bandwidth $\Delta\nu$ and angular size $\Delta\theta$ is given by

$$\langle \delta T_b^2 \rangle^{1/2} = \sigma_p(z, \Delta\nu, \Delta\theta)\beta(z)\overline{\delta T_b}(z), \quad (9)$$

where σ_p is the variance in a cylinder and β is the flux-weighted average of the halo bias.

The variance in a cylinder is given by

$$\sigma_p(z, \Delta\nu, \Delta\theta) = 2\pi \int \frac{dk_z}{k_z} \left[\frac{k_z^3 P(k_z)}{2\pi^2}\right]$$
$$\times \int_{1/R}^{\infty} dk_r \left[\frac{2}{k_r R(z)} j_0 \left(\frac{k_z L(z)}{2}\right) J_1(k_r R(z))\right]^2, \quad (10)$$

where L and R represent, respectively, the width along the line of sight and the spatial resolution of survey, $P(k)$ is the matter power spectrum and $\nu_0 = 1.42$ GHz is the rest-frame frequency for a 21 cm transition.

The flux-weighted average of the halo bias is given by

$$\beta(z) = \frac{\int_{M_{min}}^{M_{max}} b(M, z)\mathcal{F}(M)\frac{dn}{dM}dM}{\int_{M_{min}}^{M_{max}} \mathcal{F}(M)\frac{dn}{dM}dM}, \quad (11)$$

where $\mathcal{F}(M) \propto T_b r_t^2 \sigma_V$ is the effective flux from the MHs and $b(M, z)$ is the halo bias. We adopt the bias expression of Sheth, Mo & Tormen (2001) in this work. According to Iliev & Shapiro (2001), the non-linear bias approach of Scannapieco & Barkana (2002) can be robustly reproduced by the linear bias obtained in Mo & White (1996). We have checked that our choice of $b(M, z)$ closely reproduces the result using the bias of Mo & White (1996) or that of Chongchitnan & Silk (2012a) in the Gaussian case.

3 EFFECTS OF ISOCURVATURE PERTURBATIONS

As a first step in calculating the effects of isocurvature perturbations, we parametrize the primordial power spectrum for isocurvature fluctuations as

$$\mathcal{P}_{S_i}(k) \equiv \mathcal{P}_{S_i}(k_0) \left(\frac{k}{k_0}\right)^{n_s^i - 1}, \quad (12)$$

where $i = c$ or b, indicating CDM and baryon isocurvature modes. $\mathcal{P}_{S_i}(k_0)$ and $n_s^{(i)}$ are, respectively, the amplitude and the spectral index for the mode i defined at reference scale k_0. In this paper, we take $k_0 = 0.05$ Mpc^{-1}.

We define the primordial isocurvature fractions as

$$r_{cdm} \equiv \frac{\mathcal{P}_{S_c}(k_0)}{\mathcal{P}_\zeta(k_0)}, \qquad r_{bar} \equiv \frac{\mathcal{P}_{S_b}(k_0)}{\mathcal{P}_\zeta(k_0)}, \quad (13)$$

where $\mathcal{P}_\zeta(k_0)$ is the amplitude of the primordial power spectrum for the adiabatic (curvature) perturbation ζ. For simplicity, we adopt a single value for both the spectral indices of CDM and baryon isocurvature spectra, and denote this by n_s^{iso} (i.e. $n_s^c = n_s^b = n_s^{iso}$).

The total matter isocurvature perturbation, S_m is given by the combination of the isocurvature fluctuations (with respect to radiation) in CDM and in baryon (S_c and S_b), as $S_m = f_c S_c + f_b S_b$, where $f_c = \Omega_c/\Omega_m$ and $f_b = \Omega_b/\Omega_m$. It is worth noting that if CDM and baryons contribute equally to the total isocurvature fluctuations, the initial amplitude of power spectrum for the baryon mode must be larger than that of CDM by a factor of $(\Omega_c/\Omega_b)^2$.

The evolution of isocurvature fluctuations is influenced by two main factors; evolution of the metric perturbations and the amplitudes of initial fluctuations. Although the evolution of the metric perturbations is almost same between the CDM and baryon isocurvature modes, the difference in the initial fluctuations between the CDM and baryon isocurvature modes can lead to observable effects, as will be shown in this work (see also Kawasaki et al. 2011).

Let us first consider the effects of isocurvature modes on the matter power spectra. The case of a pure CDM isocurvature mode is shown in Fig. 1 at redshifts $z = 6, 10, 20$ and 40 (from left-hand column to right) with isocurvature fraction $r_{cdm} = 10^{-1}$ (dashed/green), 10^{-3} (dotted/blue) and 10^{-5} (dot–dashed/magenta), with varying spectral index $n_s^{iso} = 1, 2$ and 3 (from top row to bottom). The solid/red line in each panel shows the adiabatic spectrum.

We see that for very blue-tilted spectrum ($n_s^{iso} = 3$), the effects of the CDM isocurvature mode can be identified clearly on small scales, whereas the contribution from a scale-invariant isocurvature spectrum ($n_s^{iso} = 1$) is much smaller than the adiabatic component even with relatively large isocurvature fractions.

Fig. 2 shows the changes in the halo mass function due to the contribution from isocurvature fluctuations with respect to the adiabatic case. Each curve is derived from the corresponding matter power spectrum shown in Fig. 1, using the prescription of Press & Schechter (1974). We clearly see that the effects of the isocurvature modes are prominent on small-mass scales and at high redshifts. In particular, we see that very blue-tilted isocurvature spectra ($n_s^{iso} = 3$) exhibit very different features from the other spectra with $n_s^{iso} = 1$ or 2. The changes in the halo mass function do not vary monotonically with increasing fractional amplitudes r_{cdm}. In general, blue-tilted isocurvature spectra show enhanced fluctuations on small scales, and lead to the increase of the number of small haloes. However, if the contribution of isocurvature modes increases beyond some critical value, small haloes can become incorporated into larger haloes. This explains the unexpected features seen in the last row of Fig. 2, where the abundances of massive haloes are enhanced, but those of smaller mass haloes are suppressed. Such a feature appears in the typical mass range of MHs, i.e. $[M_{min}, M_{max}]$, and it is expected that the 21 cm signal from MHs will also exhibit such a trend.

Finally, we calculate the rms fluctuations in the 21 cm emission from MHs, $\langle \delta T_b^2 \rangle^{1/2}$, as a function of redshift (Fig. 3). Again, we assume the contribution from only the CDM type of isocurvature fluctuations. The sensitivity curves are for LOFAR, SKA and FFTT (details of the sensitivities are explained in the next section). We see that when the isocurvature spectrum is flat ($n_s^{iso}=1$), the difference in $\langle \delta T_b^2 \rangle$ compared to the adiabatic mode is $\lesssim 10^{-4}$ mK even with $r_{cdm} = 0.1$. This suggests that such isocurvature components would be extremely difficult to observe through MHs. Even with bluer isocurvature spectrum ($n_s^{iso} = 2$), the difference is still small: the model with $r_{cdm} = 0.1$ enhances the signal by not much more than a few per cent around the $z \sim 10$.

If the isocurvature spectrum is very blue ($n_s^{iso} = 3$), large differences can be seen, especially at high redshifts. However, a slight trend reversal is seen around $z \lesssim 20$, where $r_{cdm} = 10^{-3}$ boosts the signal more effectively than when $r_{cdm} = 10^{-1}$. This again can be
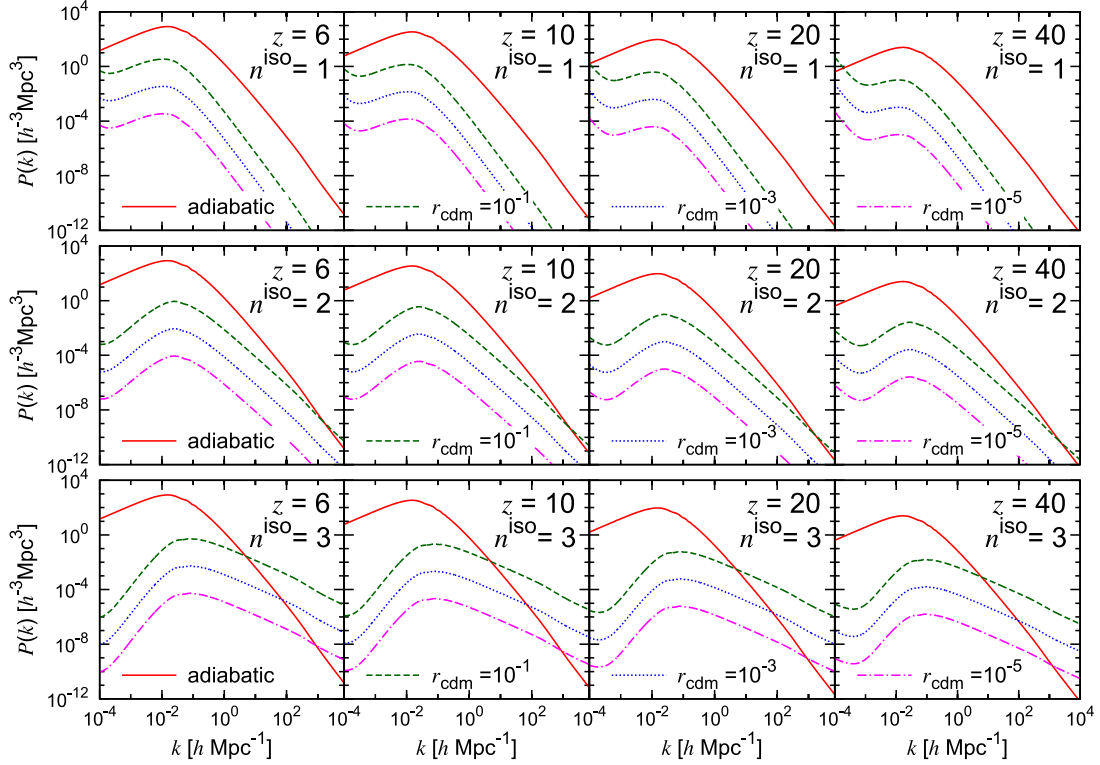
Figure 1. The matter power spectra generated by adiabatic or pure CDM isocurvature fluctuations, at redshifts $z = 6$, 10, 20 and 40 (from left-hand column to right). The spectral indices of the isocurvature mode are as $n_s^{iso} = 1$, 2 and 3 (from top row to bottom). In each panel, the different curves represent the matter power spectrum of the adiabatic fluctuations (solid/red) and the CDM isocurvature fluctuations with $r_{cdm} = 10^{-1}$ (dashed/green), 10^{-3} (dotted/blue) and 10^{-5} (dot–dashed/magenta). The isocurvature spectra shown have no contribution from adiabatic fluctuations.
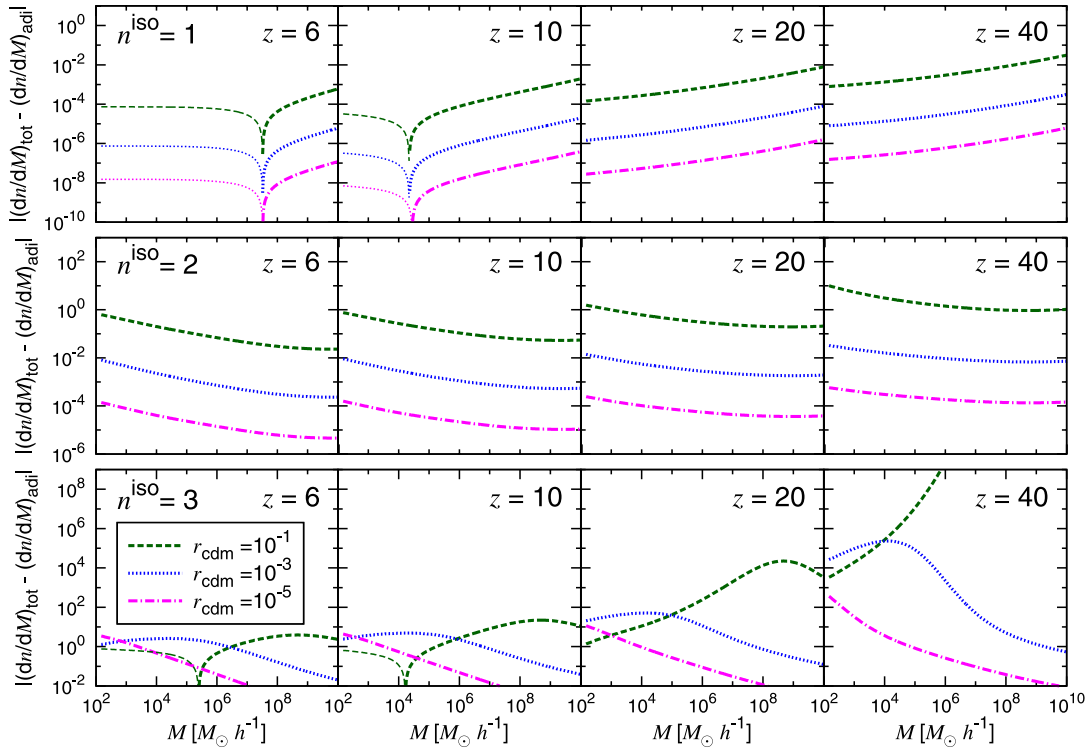
Figure 2. Deviation of the halo mass function for the case with CDM isocurvature fluctuations from the pure adiabatic case at redshifts $z = 6$, 10, 20 and 40 (from left to right). $(dn/dM)_{tot}$ represents the halo mass function for the total (adiabatic+CDM isocurvature) fluctuation; $(dn/dM)_{adi}$ is the mass function for the pure adiabatic case. Thick (thin) lines represent positive (negative) values. The spectral indices of the isocurvature perturbations are $n_s^{iso} = 1$, 2 and 3 (from top to bottom). Different line types represent different values of r_{cdm} (same as those in Fig. 1).
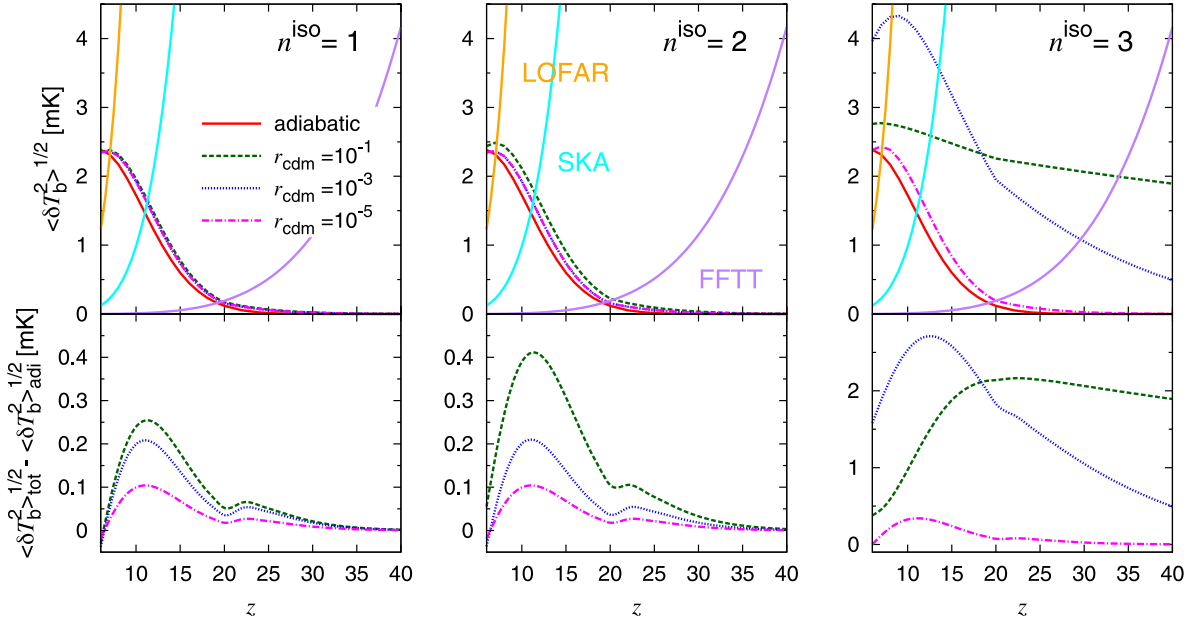
Figure 3. Top panels: the rms fluctuations in the 21 cm emission from MHs, $\langle \delta T_b^2 \rangle^{1/2}$, with the sensitivity curves for LOFAR (orange), SKA (cyan) and FFTT (purple). The curves in each panel represent the same cases as in the previous figures. Lower panels: deviation from the adiabatic case, with isocurvature spectral indices $n_s^{iso} = 1$, 2 and 3 (from left to right). $\langle \delta T_b^2 \rangle_{tot}^{1/2}$ and $\langle \delta T_b^2 \rangle_{adi}^{1/2}$, respectively, represent the signal for the case with adiabatic and CDM isocurvature fluctuations and that for the case with adiabatic fluctuations alone. The unusual trend in the last column is discussed in the text.

understood in terms of the incorporation of small-mass MHs into larger haloes, as previously discussed.

Our calculation shows that the detection of isocurvature contribution to the fluctuations in the 21 cm MH emission is possible with future telescopes such as the SKA and FFTT. If isocurvature fluctuations have a very blue spectrum with $r_{cdm} \simeq 10^{-3}$, such isocurvature signals may be detected at low redshifts even by LOFAR. However, further increase in r_{cdm} suppresses the signal at $z \lesssim 20$ due to the incorporation of small MHs into larger haloes. We shall discuss other uncertainties in the calculation of the 21 cm signal from MHs in Section 6.

4 FORECASTS

We now perform a Fisher-matrix analysis on the cosmological parameters derived from measurements of the CMB and the fluctuations in the 21 cm signal from MHs. We define the total Fisher matrix by combining the CMB and the 21 cm surveys as

$$F_{\alpha\beta} = F_{\alpha\beta}^{(CMB)} + F_{\alpha\beta}^{(21\,cm)}, \qquad (14)$$

where α, β refer to the model parameters, and $F_{\alpha\beta}^{(CMB)}$ and $F_{\alpha\beta}^{(21\,cm)}$ represent the contributions from the CMB and 21 cm observations. We adopt following 12 parameters in our analysis:

$$\boldsymbol{p} = \{\Omega_b h^2, \ \Omega_c h^2, \ \Omega_\Lambda, \ \tau^{reion}, \ n_s, \ A_s, \ w, \ Y_p, \ \alpha_s, \ r_{cdm}, r_{bar}, \ n_s^{iso}\}, \qquad (15)$$

where Ω_b, Ω_c and Ω_Λ are the density parameters for baryons, CDM and cosmological constant, respectively; h is the dimensionless Hubble constant; w is the equation of state for dark energy; Y_p is the primordial abundance of Helium; τ^{reion} is the optical depth at the EoR;[5] n_s and A_s are the spectral index and the amplitude of

the primordial power spectrum for the adiabatic mode; α_s is the running of the spectral index; r_{cdm} and r_{bar} are CDM and baryon isocurvature fractions; n_s^{iso} is the spectral index for the isocurvature perturbations.

4.1 CMB Fisher matrix

The Fisher matrix for a CMB survey is given by (Tegmark, Taylor & Heavens 1997)

$$F_{\alpha\beta}^{(CMB)} = f_{sky}^{CMB} \sum_{\ell=2}^{l_{max}} \frac{2\ell+1}{2} \mathrm{Tr} \left[\mathbf{C}_{\ell;\alpha} \mathbf{C}_\ell^{-1} \mathbf{C}_{\ell;\beta} \mathbf{C}_\ell^{-1} \right], \qquad (16)$$

where f_{sky}^{CMB} is the sky coverage of the CMB survey, $\mathbf{C}_\ell$ is the covariance matrix and $\mathbf{C}_{\ell;\alpha}$ represents its derivative with respect parameter p_α; $\mathbf{C}_{\ell;\alpha} \equiv \partial \mathbf{C}_\ell / \partial p_\alpha$. The CMB observables include the temperature anisotropies (T), the E-mode polarization (E) and the CMB lensing potential (ψ). The covariance matrix constructed from these observables is given by

$$\mathbf{C}_\ell \equiv \begin{pmatrix} C_\ell^{TT} + N_\ell^{TT} & C_\ell^{TE} & C_\ell^{T\psi} \\ C_\ell^{TE} & C_\ell^{EE} + N_\ell^{EE} & C_\ell^{E\psi} \\ C_\ell^{T\psi} & C_\ell^{E\psi} & C_\ell^{\psi\psi} + N_\ell^{\psi\psi} \end{pmatrix}, \qquad (17)$$

where C_ℓ and N_ℓ represent the angular power spectrum and the noise spectrum, respectively. For simplicity, we assume that the cross-correlation between the E-mode polarization and the CMB lensing potential can be neglected (i.e. $C_\ell^{E\psi} = 0$).[6]

---

[5] We treat τ^{reion} as a model parameter only in the CMB measurement since τ^{reion} does not affect the 21 cm signals in our analysis.

[6] This is because E-mode polarization is generated via Thomson scattering around the last-scattering surface, whereas the sources of CMB lensing are the large-scale structures between us and the last scattering surface. However, such correlation, though small, is not exactly zero since the E-mode polarization can also be generated during the EoR, and structures in this era can also act as lensing sources (Lewis, Challinor & Hanson 2011).

Table 1. The specifications for a mid-cost *CMBPol* (EPIC-2m type) mission adopted in this paper. Here ν refers to the frequency of each channel, θ_{FWHM} is the angular resolution, Δ_ν^T and Δ_ν^P are the sensitivities for the temperature and polarization measurements.

ν (MHz)	θ_{FWHM} (arcmin)	Δ_ν^T (μK arcmin)	Δ_ν^P (μK arcmin)
45	17	5.85	8.27
70	11	2.96	4.19
100	8	2.29	3.24
150	5	2.21	3.13
220	3.5	3.39	4.79

The noise spectrum for a CMB experiment is given by (Knox 1995)

$$N_\ell^{T,P} = \left[\sum_\nu \left\{ \left(\Delta_\nu^{T,P} \theta_{\mathrm{FWHM}} \right)^2 e^{-\ell(\ell+1)\theta_{\mathrm{FWHM}}^2/8\ln 2} \right\}^{-1} \right]^{-1}, \quad (18)$$

where $\Delta_\nu^{T,P}$ denotes the sensitivity of the temperature or polarization measurement and θ_{FWHM} represents the angular resolution (the so-called full width at half-maximum). We calculate the noise spectrum for the lensing-potential measurement using the formalism outlined in Hu & Okamoto (2002) and Okamoto & Hu (2003). In particular, we assume the projected sensitivities of the *CMBPol* mission (Baumann et al. 2009), with $f_{\mathrm{sky}}^{\mathrm{CMB}}=1$ and $\ell_{\mathrm{max}}=4000$. We use specifications for a mid-cost *CMBPol* (EPIC-2m type) mission, as shown in Table 1.

4.2 21 cm Fisher matrix

For a 21 cm survey, we define the Fisher matrix as

$$F_{\alpha\beta}^{(21\,\mathrm{cm})} = f_{\mathrm{sky}}^{21\,\mathrm{cm}} \sum_i \sum_{\mathrm{pixel}} \left(\frac{\partial S^i}{\partial p_\alpha} \right) \frac{1}{2(S^i + N^i)^2} \left(\frac{\partial S^i}{\partial p_\beta} \right), \quad (19)$$

where i runs over all redshift slices, $f_{\mathrm{sky}}^{21\,\mathrm{cm}}$ is the sky coverage for the 21 cm survey, S^i and N^i represent the signal and noise in the ith redshift slice. We define the signal and the noise as $S^i \equiv \langle \delta T_b^2(z_i) \rangle^{1/2}$ and $N^i \equiv \delta T_N(z_i)$, respectively, and $\delta T_N(z)$ is given by (Furlanetto, Oh & Briggs 2006)

$$\delta T_N(z) = 20 \text{ mK} \frac{10^4 \mathrm{m}^2}{A_{\mathrm{tot}}} \left[\frac{10'}{\Delta\theta} \right]^2 \left[\frac{1+z}{10} \right]^{4.6} \left[\frac{\mathrm{MHz}}{\Delta\nu} \frac{100\,h}{t_{\mathrm{int}}} \right]^{1/2}, \quad (20)$$

where A_{tot} is the effective collecting area of the radio array, $\Delta\theta$ is the angular resolution, $\Delta\nu$ is the frequency bandwidth and t_{int} is the total integration time. The sensitivity curves shown in Fig. 3 assume $A_{\mathrm{tot}} = 10^4$ m^2 (LOFAR), $A_{\mathrm{tot}} = 10^5$ m^2 (SKA) and $A_{\mathrm{tot}} = 10^7$ m^2 (FFTT), with $t_{\mathrm{int}} = 1000$ h in all cases.

As a fiducial survey, we use the specifications of FFTT, with $A_{\mathrm{tot}} = 10^7$ m^2, $\Delta\theta = 9$ arcmin, $\Delta\nu = 1$ MHz and $t_{\mathrm{int}} = 1000$ h.

5 RESULTS

5.1 The $r_{\mathrm{cdm}} - r_{\mathrm{bar}}$ plane

Fig. 4 summarizes the results from our Fisher analysis. The contours show the projected 1σ (68 per cent) and 2σ (95 per cent) constraints in the $r_{\mathrm{cdm}} - r_{\mathrm{bar}}$ plane expected from *CMBPol* alone and from combining with either the SKA or FFTT. We perform the analysis over the redshift range $6 \leq z \leq 40$ in equally spaced bins centred at z_i with bin separation $\Delta z_i = 1$. Within each bin, we assume the bandwidth resolution of $\Delta\nu = 1$ MHz.

As shown in the previous section, the contribution from a scale-invariant ($n_s^{\mathrm{iso}} = 1$) isocurvature spectrum to the 21 cm MH signal is small. This is also evident from the contours, which are only modestly tightened by when 21 cm constraints are added to those from *CMBPol*. The improvement is more dramatic for bluer isocurvature spectra, especially in the bottom-right panel, where we can see that
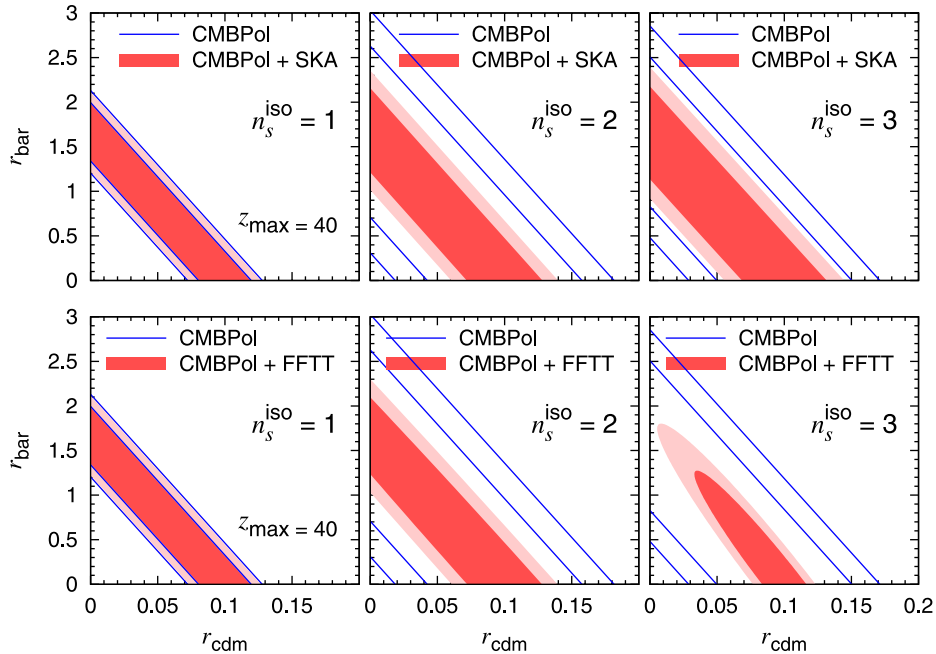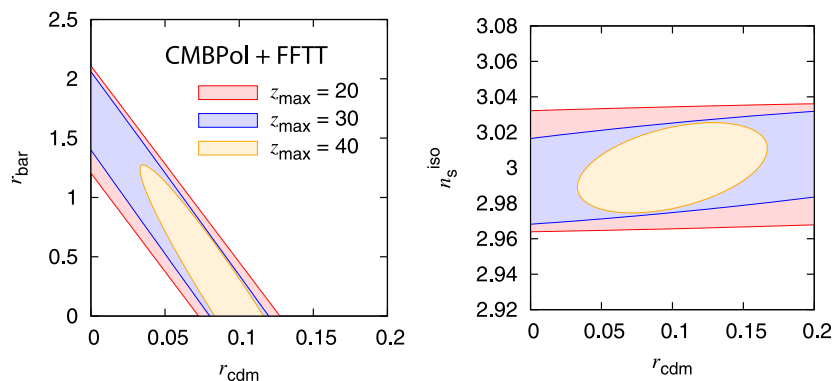

Figure 4. Projected 1σ (68 per cent) and 2σ (95 per cent) constraints in the $r_{\mathrm{cdm}} - r_{\mathrm{bar}}$ plane from the CMB alone (solid/blue line) and CMB+21 cm (shaded/red region). We assume *CMBPol* specifications and the SKA (top panels) or FFTT (bottom panels) for the observation of 21 cm MH signal. For the fiducial model, we used $n_s^{\mathrm{iso}} = 1$, 2 and 3 (from left to right), and the fiducial isocurvature fractions are $(r_{\mathrm{cdm}}, r_{\mathrm{bar}}) = (0.1, 0)$ in all cases.

it is possible to break parameter degeneracies by the combining CMB and 21 cm constraints. Comparing the constraints from SKA and FFTT, both sets of constraints show similar results, except in the case with $n_s^{iso} = 3$, where the constraint from FFTT is clearly much tighter than that from the SKA.

The constraint on the case with $n_s^{iso} = 3$ from a combination of *CMBPol* and FFTT shows larger error of r_{bar} than that of r_{cdm}. The difference of the amplitude of errors between CDM and baryon isocurvature fluctuations comes from the fact that the baryon isocurvature fluctuations are required the larger amplitude by a factor of $(\Omega_c/\Omega_b)^2$ to realize the same amount of isocurvature fluctuations with that of CDM.

5.2 Dependence on z_{max}

Next, we consider the dependence of the constraints on the redshift range used in the Fisher analysis. Fig. 5 shows the 1σ contours expected from *CMBPol*+FFTT, where the maximum redshift varies

from $z_{max} = 20$ to 40. We show the results in both the $r_{cdm}-r_{bar}$ and the $r_{cdm}-n_s^{iso}$ planes. The contours suggest that if information up to $z_{max} \sim 40$ can be utilized, there is some hope of differentiating the CDM and baryon isocurvature perturbations. Incidentally, we noted that the constraints from the SKA are saturated when $z_{max} \sim 20$, beyond which point the signal-to-noise ratio for the SKA falls below 1.

5.3 Information in redshift slices

We further investigate the information content in each redshift slice, to determine which redshifts constrain the isocurvature perturbations most effectively. In Fig. 6, we plot the diagonal components for the inverse Fisher matrix, $(\mathbf{F}^{-1})_{\alpha\alpha}$, in the cases when the errors are marginalized (top row) and unmarginalized (bottom row), with $\alpha = r_{cdm}$, r_{bar} and n_s^{iso}. The 21 cm survey is again taken to be the FFTT, and we use the *CMBPol* prior in each redshift slice.

Figure 5. The effects of varying z_{max} (maximum redshifts probed by the 21 cm experiment) on the 1σ constraints from the *CMBPol*+FFTT in the $r_{cdm}-r_{bar}$ plane (left-hand panel) and the $r_{cdm}-n_s^{iso}$ plane (right). The fiducial model is the adiabatic model plus CDM isocurvature with $r_{cdm} = 0.1$ and $n_s^{iso} = 3$. Different colour contours represent different values of z_{max}, where $z_{max} = 20$ (outer/red), 30 (middle/blue) and 40 (inner/orange).
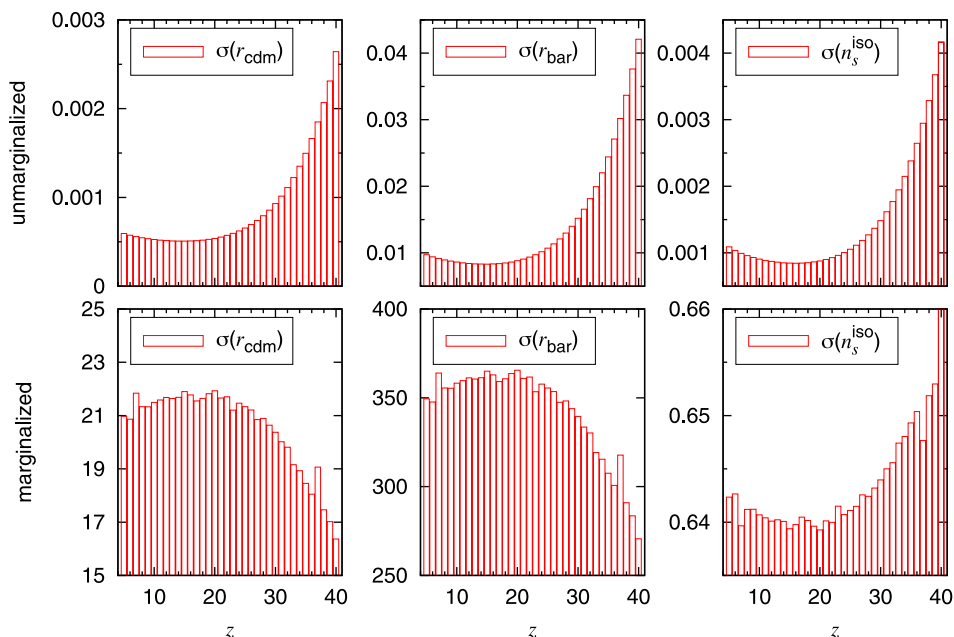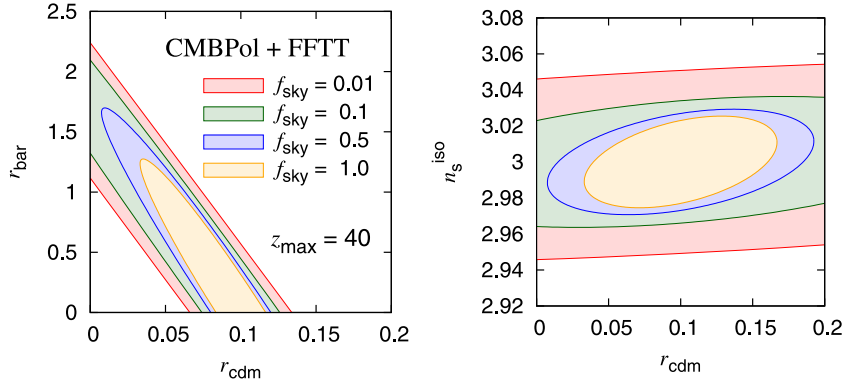

Figure 6. The unmarginalized (top panels) and marginalized (bottom panels) 1σ errors in each redshift slice. The fiducial model is the adiabatic model plus CDM isocurvature fluctuations with $(r_{cdm}, r_{bar}) = (0.1, 0)$ and $n_s^{iso} = 3.0$, and specifications of *CMBPol*+FFTT are assumed. The spatial and frequency resolutions are $\Delta\theta = 9$ arcmin and $\Delta\nu = 1$ MHz, respectively. The observed trends are discussed in the text.

Figure 7. The effects of varying f_{sky} on the projected 68 per cent CL isocurvature constraints from *CMBPol*+FFTT, where $f_{sky} = 0.01$ (outermost/red), 0.1 (green), 0.5 (blue) and 1.0 (innermost/orange). The fiducial model is the adiabatic model plus CDM isocurvature fluctuations with $r_{cdm} = 0.1$ and $n_s^{iso} = 3$, and $z_{max} = 40$.

For the unmarginalized error, the minimum of the 1σ errors appears around $z = 20$, which is slightly higher than the peaks of the 21 cm signal from MHs ($z \sim 10$). This is because the effects of isocurvature modes are more prominent at higher redshifts. On the other hand, the marginalized errors show the opposite trends from the unmarginalized errors for r_{cdm} and r_{bar}. This is due to the strong degeneracy between CDM and baryon isocurvature modes, as well as degeneracies with the other cosmological parameters. As discussed in Kawasaki et al. (2011), the differences between CDM and baryon isocurvature modes become more distinct on large scales. Since observations at higher redshift include larger correlation lengths with the same angular scale, the marginalized errors in r_{cdm} and r_{bar} are reduced with increasing redshift.

5.4 Dependence on f_{sky}

Finally, we examine the dependence of the isocurvature constraints on the sky coverage. We compare the constraints from the fluctuations in the 21 cm MH emission using $f_{sky} = 0.01, 0.1, 0.5$ and 1, and show the 1σ error contours in Fig. 7. The constraints in both the $r_{cdm}-r_{bar}$ plane (left-hand panel) and the $r_{cdm}-n_s^{iso}$ plane (right) are shown.

We see that in order to rule out $r_{cdm} = 0$ with 68 per cent confidence, more than half the sky must be surveyed using the combined *CMBPol* and FFTT and probing MHs up to $z_{max} = 40$. We also see that the spectral index n_s^{iso} can be constrained with accuracy up to a few per cent if f_{sky} is at least 0.1.

6 DISCUSSIONS

MHs are generally small, non-linear objects and their dynamics are governed by non-linearity on small scales. *N*-body simulations are, therefore, the most reliable way to study their dynamics. It is, however, a challenging task to resolve small MHs in *N*-body simulations (see e.g. Shapiro, Iliev & Raga 2004; Richardson, Scannapieco & Gray 2013 for previous simulations).

Following (Chongchitnan & Silk 2012b), we now discuss two additional factors concerning MH dynamics which may affect the results presented in the previous section; (i) uncertainty in the halo mass function and (ii) uncertainty of mass range of MHs. Our results are summarized in Figs 8 and 9.

6.1 Uncertainty in the mass function

The left-hand column of Fig. 8 shows the 21 cm fluctuations for $(r_{cdm}, r_{bar}) = (0.1, 0)$ (top) and $(r_{cdm}, r_{bar}) = (10^{-3}, 0)$ (bottom) using various prescriptions for the halo mass functions, namely, (Press & Schechter 1974, hereafter PS), (Sheth & Tormen 1999, hereafter ST), Tinker et al. (2008) and Warren et al. (2006).

We see that when the isocurvature fraction is small ($r_{cdm} = 10^{-3}$), the PS and Tinker prescriptions give similarly high amplitudes of the signal from MHs, whereas the Warren and ST prescriptions both give lower amplitudes. The trends are reversed for high redshifts. These behaviours agree with those found by Chongchitnan & Silk (2012b). When the isocurvature fraction is large ($r_{cdm} = 0.1$), the PS prescription shows an unexpectedly low 21 cm signal at $z \lesssim 10$. Nevertheless, these mass functions generally predict similar trends and amplitudes that do not differ significantly.

The left-hand column in Fig. 9 shows the 1σ contours in the $r_{cdm}-r_{bar}$ plane (top) and the $r_{cdm}-n_s^{iso}$ plane (bottom) using *CMBPol*+FFTT, when different mass functions are adopted. We observe that mass functions which predict larger amplitudes of $\langle \delta T_b^2 \rangle^{1/2}$ show relatively tighter constraints, as one might expect. The PS mass function shows a particularly tight constraint in the $n_s^{iso}-r_{cdm}$ plane, and one could interpret this as an overestimation of the constraining power of the MHs on isocurvature parameters when the PS formalism is used.

6.2 Uncertainty in M_{min}

Another uncertainty is the mass range $[M_{min}, M_{max}]$ of MHs. Whilst we have so far taken M_{min} to be the Jeans mass, M_J, large relative velocities between dark matter and baryons can cause the advection of baryons out of dark matter potential and result in $M_{min} > M_J$ (Tseliakhovich, Barkana & Hirata 2011; McQuinn & O'Leary 2012). The uncertainty in M_{max} is, in comparison, far less serious since the sharp decline in the halo mass function ensures that the number of very massive MHs is suppressed.

The 21 cm signal from MHs using $M_{min} = 10, 50$ and 100 times the Jeans mass are shown in the right-hand column of Fig. 8. We see that the increasing M_{min} suppresses the signal over all redshifts, with the suppression more prominent at higher redshifts. This is, of course, due to the reduction in the number of MHs. The right-hand column in Fig. 9 shows the corresponding effects on the 1σ constraints, which, as expected, become poorer when M_{min} is increased.
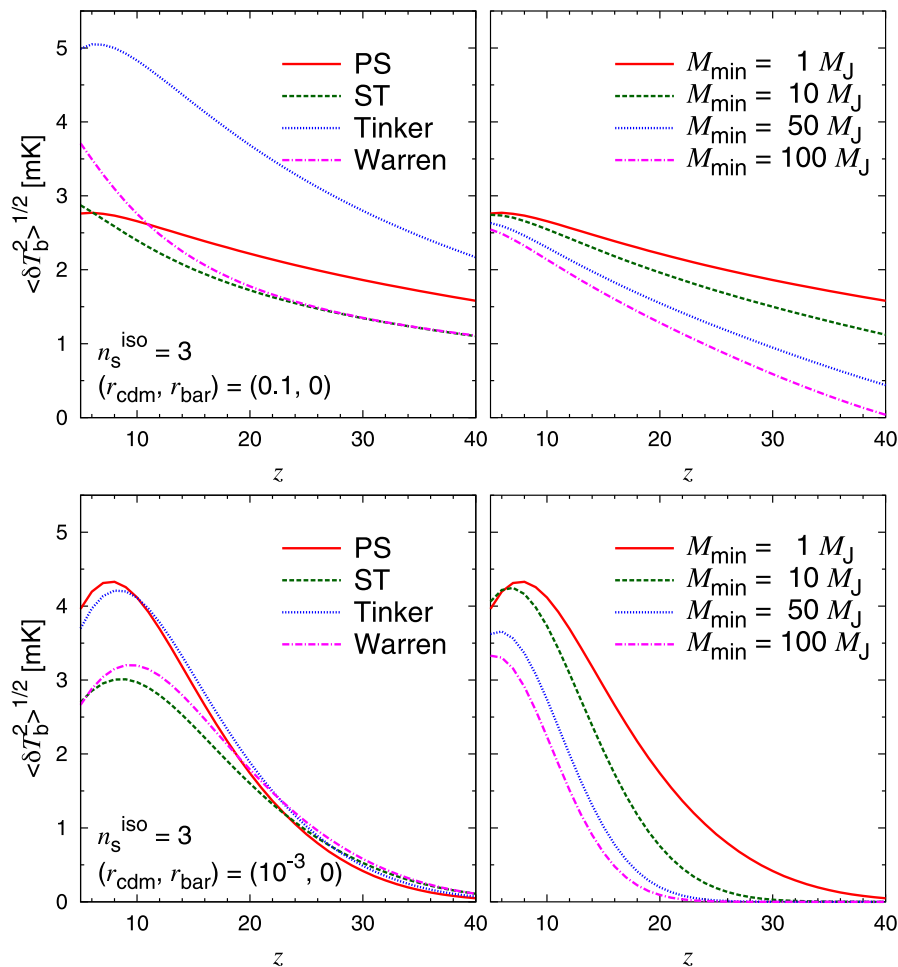
Figure 8. The effects of changing the halo mass function (left) or the minimum mass of MHs, M_{min} (right), on the fluctuations in the 21 cm emission from MHs. Top panels show the cases with large CDM isocurvature fraction ($r_{cdm} = 0.1$) whilst the lower panels show the cases with $r_{cdm} = 10^{-3}$.

There are of course other uncertainties in the theoretical modelling of MHs which have not been pursued here, including the interaction of MHs with external UV sources through Lyα pumping (Chongchitnan & Silk 2012b), as well as deviations of MHs from the TIS profile. Indeed, dark matter and gas in MHs could possibly take on different, more complex profiles than those postulated by the TIS model. A more numerical approach than presented here would be required however (see e.g. Ricotti, Pontzen & Viel 2007; Ricotti 2009).

7 CONCLUSIONS

We have investigated the effects of isocurvature perturbations on the 21 cm emission from MHs at high redshifts. Our results showed that if the isocurvature power spectrum is flat ($n_s^{iso} \approx 1$), the 21 cm MH signal (as measured by the rms differential brightness temperature) changes only by less than a few per cent around its peak. However, strongly blue-tilted spectrum ($n_s^{iso} \approx 3$) gives rise to a significant increase in the amplitude of the 21 cm signal compared with the adiabatic case. The next generation of large radio telescopes such as the SKA and FFTT has the potential to detect these 21 cm imprints from a blue isocurvature spectrum.

The characteristic signatures of isocurvature perturbations on the MH abundances were explored in detail. In particular, we found an unexpected deficit in small-mass MHs when the isocurvature fraction increases beyond a certain threshold. We explained this phenomenon in terms of the incorporation of small-mass MHs into larger haloes.

A detailed Fisher-matrix analysis was performed to study quantitatively how the 21 cm signals from MHs can constrain the isocurvature amplitude and spectral index. We found that if the isocurvature spectrum is flat, (1) the combination of CMB and 21 cm experiments fares no better than the CMB alone and (2) the CDM and baryon types of isocurvature fluctuations are unlikely to be distinguishable, even with the futuristic *CMBPol*+FFTT specifications. However, if $n_s^{iso} \approx 3$, there are realistic prospects for distinguishing between different isocurvature types, but only if the 21 cm signal from redshifts up to ~40 can be utilized. Some physical models which predict very blue isocurvature spectrum with $n_s^{iso} = 2-4$ are discussed in Kasuya & Kawasaki (2009).

Two sources of uncertainty in the MH population were discussed, namely, the halo mass function and the mass range of MHs. The amplitudes of the 21 cm emission from MHs were shown to be fairly sensitive to the halo mass function, although signals from a blue spectrum remain strong enough to be detected by the SKA and FFTT regardless of the mass function. We also explored the uncertainty in the minimum MH mass, and showed that increasing M_{min} suppresses the 21 cm signal over a large range of redshifts, especially at high redshifts where an order-of-magnitude suppression was seen.
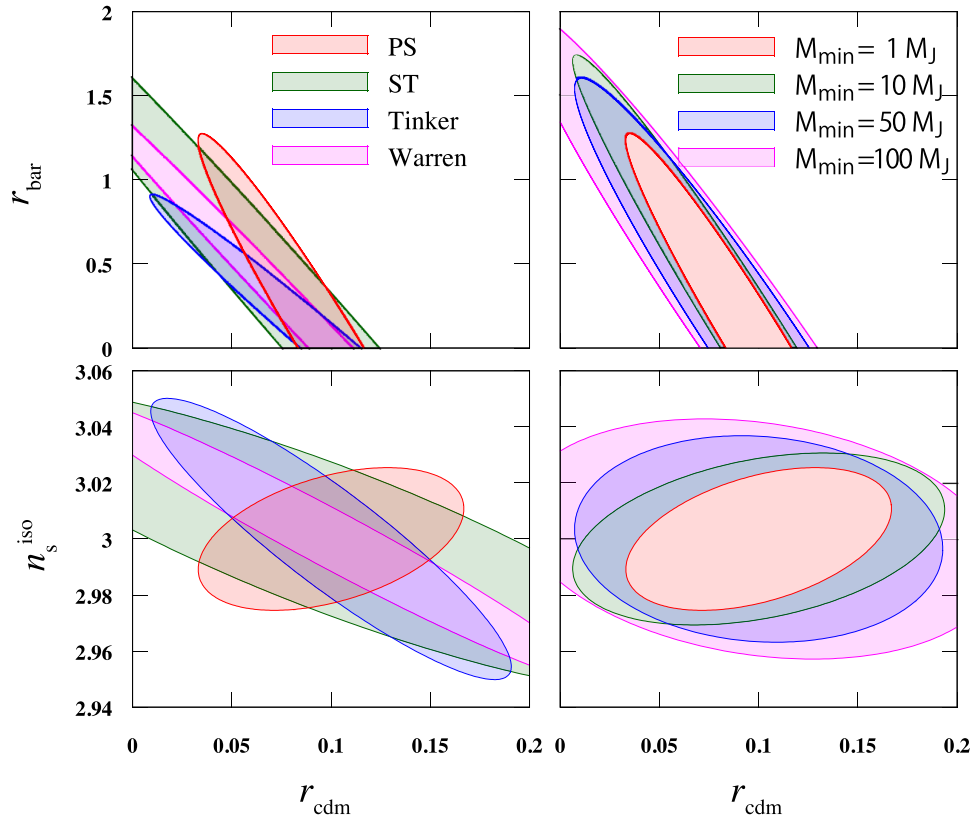
Figure 9. The effects of changing the halo mass function (left) or the minimum mass of MHs, M_{min} (right), on the projected 1σ constraints in the $r_{cdm}-r_{bar}$ plane (top) and the $r_{cdm}-n_s^{iso}$ plane (bottom).

For the two sources of uncertainty above, we also obtained the error contours in the $r_{cdm}-r_{bar}$ and the $r_{cdm}-n_s^{iso}$ planes. These constraints are sensitive to the choice of the mass function: the Press–Schechter prescription, in particular, can be construed as giving overly optimistic constraints. Increasing M_{min} suppresses the MH signal strongly at high redshifts, hence the error contours are also significantly widened.

In summary, the fluctuations of the 21 cm emission from MHs are a viable tool in the search for isocurvature perturbations, and have the potential to rule out inflation models which predict a very blue-tilted isocurvature spectrum. When combined with CMB constraints, future 21 cm experiments have the potential to distinguish between the CDM and baryon types of isocurvature perturbations. This will be extremely useful in the understanding of physics in the inflationary era.

Our analysis focused on uncorrelated CDM and baryon isocurvature modes, but it is plausible that there may be a non-trivial correlation between the two. Such a correlation gives rise to additional degrees of freedom. In future work, it will be interesting to explore the parameter space allowed by certain inflationary theories which predict correlated isocurvature modes.

Note added. Prior to the publication of this work, we became aware of the work by Sekiguchi et al. (2013), which significantly overlaps with our work. The conclusions in their work are similar to ours.

ACKNOWLEDGEMENTS

REFERENCES

Bardeen J. M., 1980, Phys. Rev. D, 22, 1882
Barkana R., Loeb A., 2005, MNRAS, 363, L36
Baumann D. et al., 2009, AIP Conf. Ser. Vol. 1141, Probing Inflation with CMB Polarization. Am. Inst. Phys., New York, p. 10
Beltran M., 2008, Phys. Rev. D, 78, 023530
Bennett C. L. et al., 2013, ApJS, 208, 20
Brandenburg A., Steffen F. D., 2004, J. Cosmol. Astropart. Phys., 0408, 008
Bucher M., Moodley K., Turok N., 2000, Phys. Rev. D, 62, 083508
Chongchitnan S., Silk J., 2012a, Phys. Rev. D, 85, 063508
Chongchitnan S., Silk J., 2012b, MNRAS, 426, L21
Covi L., Kim H.-B., Kim J. E., Roszkowski L., 2001, J. High Energy Phys., 0105, 033
Covi L., Roszkowski L., Small M., 2002, J. High Energy Phys., 0207, 023
Dvali G., Gruzinov A., Zaldarriaga M., 2004, Phys. Rev. D, 69, 023505
Field G. B., 1958, Proc. IRE, 46, 240
Furlanetto S. R., Loeb A., 2002, ApJ, 579, 1
Furlanetto S., Oh S. P., Briggs F., 2006, Phys.Rep., 433, 181
Gordon C., Pritchard J. R., 2009, Phys. Rev. D, 80, 063535
Hinshaw G. et al., 2013, ApJS, 208, 19
Hu W., Okamoto T., 2002, ApJ, 574, 566

Ichikawa K., Suyama T., Takahashi T., Yamaguchi M., 2008a, Phys. Rev. D, 78, 023513
Ichikawa K., Suyama T., Takahashi T., Yamaguchi M., 2008b, Phys. Rev. D, 78, 063545
Iliev I. T., Shapiro P. R., 2001, MNRAS, 325, 468
Iliev I. T., Shapiro P. R., Ferrara A., Martel H., 2002, ApJ, 572, L123
Kasuya S., Kawasaki M., 2009, Phys. Rev. D, 80, 023516
Kawasaki M., Sekiguchi T., Takahashi T., 2011, J. Cosmol. Astropart. Phys., 10, 28
Knox L., 1995, Phys. Rev. D, 52, 4307
Kodama H., Sasaki M., 1984, Prog. Theor. Phys. Suppl., 78, 1
Kofman L., 2003, preprint (astro-ph/0303614)
Langlois D., Vernizzi F., 2004, Phys. Rev. D, 70, 063522
Langlois D., Vernizzi F., Wands D., 2008, J. Cosmol. Astropart. Phys., 0812, 004
Lazarides G., de Austri R. R., Trotta R., 2004, Phys. Rev. D, 70, 123527
Lewis A., Challinor A., 2007, Phys. Rev. D, 76, 083005
Lewis A., Challinor A., Hanson D., 2011, J. Cosmol. Astropart. Phys., 3, 18
Lyth D. H., Wands D., 2003, Phys. Rev. D, 68, 103515
Lyth D. H., Ungarelli C., Wands D., 2003, Phys. Rev. D, 67, 023503
Madau P., Meiksin A., Rees M. J., 1997, ApJ, 475, 429
McQuinn M., O'Leary R. M., 2012, ApJ, 760, 3
Mo H. J., White S. D. M., 1996, MNRAS, 282, 347
Moroi T., Takahashi T., 2002, Phys. Rev. D, 66, 063501
Moroi T., Takahashi T., 2005, Phys. Rev. D, 72, 023505
Moroi T., Takahashi T., 2009, Phys. Lett., B671, 339
Moroi T., Takahashi T., Toyoda Y., 2005, Phys. Rev. D, 72, 023502
Okamoto T., Hu W., 2003, Phys. Rev. D, 67, 083002

Planck Collaboration, 2013a, preprint (arXiv:1303.5062)
Planck Collaboration, 2013b, preprint (arXiv:1303.5082)
Planck Collaboration, 2013c, preprint (arXiv:1303.5076)
Press W. H., Schechter P., 1974, ApJ, 187, 425 (PS)
Rajagopal K., Turner M. S., Wilczek F., 1991, Nucl. Phys. B, 358, 447
Richardson M. L. A., Scannapieco E., Gray W. J., 2013, ApJ, 778, 80
Ricotti M., 2009, MNRAS, 392, L45
Ricotti M., Pontzen A., Viel M., 2007, ApJ, 663, L53
Scannapieco E., Barkana R., 2002, ApJ, 571, 585
Sekiguchi T., Tashiro H., Silk J., Sugiyama N., 2013, preprint (arXiv:1311.3294)
Shapiro P. R., Iliev I. T., Raga A. C., 1999, MNRAS, 307, 203
Shapiro P. R., Iliev I. T., Raga A. C., 2004, MNRAS, 348, 753
Sheth R. K., Tormen G., 1999, MNRAS, 308, 119 (ST)
Sheth R. K., Mo H. J., Tormen G., 2001, MNRAS, 323, 1
Takahashi T., Yamaguchi M., Yokoyama S., 2009a, Phys. Rev. D, 80, 063524
Takahashi T., Yamaguchi M., Yokoyama J., Yokoyama S., 2009b, Phys. Lett. B, 678, 15
Tashiro H., Sekiguchi T., Silk J., 2013, J. Cosmol. Astropart. Phys., 01, 013
Tegmark M., Zaldarriaga M., 2009, Phys. Rev. D, 79, 083530
Tegmark M., Taylor A. N., Heavens A. F., 1997, ApJ, 480, 22
Tinker J., Kravtsov A. V., Klypin A., Abazajian K., Warren M., Yepes G., Gottlöber S., Holz D. E., 2008, ApJ, 688, 709
Tseliakhovich D., Barkana R., Hirata C. M., 2011, MNRAS, 418, 906
Warren M. S., Abazajian K., Holz D. E., Teodoro L., 2006, ApJ, 646, 881

This paper has been typeset from a TEX/LATEX file prepared by the author.